Toward detecting polycyclic aromatic hydrocarbons on planetary objects with ORIGIN

Kipfer, K.A.; Ligterink, N.F.W.; Bouwman, J.; Schwander, L.; Grimaudo, V.; Koning, C.P. de; ... ; Riedo, A.

The Planetary Science Journal, 3:43 (16pp), 2022 February https://doi.org/10.3847/PSJ/ac4e15

Toward Detecting Polycyclic Aromatic Hydrocarbons on Planetary Objects with ORIGIN

K. A. Kipfer[1], N. F. W. Ligterink[1], J. Bouwman[2,3,4,5], L. Schwander[1], V. Grimaudo[1], C. P. de Koning[1], N. J. Boeren[1,6], P. Keresztes Schmidt[1], R. Lukmanov[1], M. Tulej[1], P. Wurz[1], and A. Riedo[1]
[1] Space Research and Planetary Sciences, Physics Institute, University of Bern, 3012 Bern, Switzerland; kristina.kipfer@unibe.ch, andreas.riedo@unibe.ch
[2] Laboratory for Astrophysics, Leiden Observatory, Leiden University, P.O. Box 9513, 2300 RA Leiden, The Netherlands
[3] Present address: Laboratory for Atmospheric and Space Physics, University of Colorado, Boulder, CO 80303, USA
[4] Present address: Department of Chemistry, University of Colorado, Boulder, CO 80309, USA
[5] Present address: Institute for Modeling Plasma, Atmospheres, and Cosmic Dust (IMPACT), University of Colorado, Boulder, CO 80303, USA
[6] NCCR PlanetS, University of Bern, 3012 Bern, Switzerland
Received 2021 September 16; revised 2022 January 18; accepted 2022 January 19; published 2022 February 18

Abstract

Polycyclic aromatic hydrocarbons (PAHs) are found on various planetary surfaces in the solar system. They are proposed to play a role in the emergence of life, as molecules that are important for biological processes could be derived from them. In this work, four PAHs (pyrene, perylene, anthracene, and coronene) were measured using the ORganics Information Gathering INstrument system (ORIGIN), a lightweight laser desorption ionization-mass spectrometer designed for space exploration missions. In this contribution, we demonstrate the current measurement capabilities of ORIGIN in detecting PAHs at different concentrations and applied laser pulse energies. Furthermore, we show that chemical processing of the PAHs during measurement is limited and that the parent mass can be detected in the majority of cases. The instrument achieves a 3σ detection limit in the order of femtomol mm^{-2} for all four PAHs, with the possibility of further increasing this sensitivity. This work illustrates the potential of ORIGIN as an instrument for the detection of molecules important for the emergence or presence of life, especially when viewed in combination with previous results by the instrument, such as the identification of amino acids. ORIGIN could be used on a lander or rover platform for future in situ missions to targets in the solar system, such as the icy moons of Jupiter or Saturn.

Unified Astronomy Thesaurus concepts: Mass spectrometry (2094); Polycyclic aromatic hydrocarbons (1280); Space vehicle instruments (1548); Mass spectrometers (1013); Laboratory astrophysics (2004); Astrochemistry (75)

1. Introduction

More than 240 molecular species have been unambiguously detected in the circumstellar and interstellar medium (ISM; McGuire 2021), the majority of which contain at least one atom of carbon. One important family of carbon-bearing molecules in the ISM is the polycyclic aromatic hydrocarbons (PAHs). The PAHs are detected in the ISM through the characteristic mid-infrared bands that they emit after being excited by interstellar visible and UV radiation (Leger & Puget 1984; Allamandola et al. 1985). Based on the aromatic infrared bands, it was estimated that 10%–25% of all interstellar carbon is locked up in PAHs (Tielens 2008, 2013). The PAHs are thought to be efficiently formed in the outflows of carbon-rich stars (Cherchneff et al. 1992; Cherchneff 2011; Joblin et al. 2011) through processes similar to those responsible for PAH formation in terrestrial combustion reactions (Frenklach & Feigelson 1989; Yang et al. 2017; McCabe et al. 2020).

A wealth of spectroscopic data of PAHs and their cations has been recorded in the infrared for PAHs isolated in solid noble gas matrices (Szczepanski & Vala 1993; Hudgins & Sandford 1998) and the gas phase (Oomens et al. 2001; Maltseva et al. 2018; Bouwman et al. 2020, 2021) and embedded in water ice (Gudipati & Allamandola 2004; Bouwman et al. 2010). Furthermore, PAHs and their cations are considered prominent candidates to explain the diffuse interstellar bands (Salama & Allamandola 1992; Ruiterkamp et al. 2005). Therefore, their UV–VIS spectra in solid noble gas matrices and the gas phase have also been studied in great detail (Salama & Allamandola 1991; Salama et al. 1999, 2011; Ruiterkamp et al. 2002; Halasinski et al. 2005; Bouwman et al. 2011; Gredel et al. 2011; Steglich et al. 2011; Salama & Ehrenfreund 2013; Huisken et al. 2014). Despite the extensive spectroscopic studies, secure identification of specific PAH molecules in the ISM via spectroscopy has proven to be difficult and is currently limited to detections of 1- and 2-cyanonaphthalene using microwave spectroscopy (McGuire et al. 2021).

The PAHs are of interest not only because of their abundance in the ISM but also due to their potential role in the emergence of life. Although PAHs are not synthesized directly by biological processes (Sephton et al. 2018), they could be precursors of molecules important for life (Ehrenfreund et al. 2006). For example, derivatives of pyrene and anthracene, as well as derivatives of other PAHs, were found to have a stabilizing influence on fatty acid membranes, therefore possibly functioning as cholesterol analogs in prebiotic single-chain amphiphilic membranes (Groen et al. 2012). The UV photolysis of interstellar ice analogs containing PAHs can add chemical side groups, which have been formed via the products of photolysis of other ice constituents (Bernstein et al. 2002; Allamandola 2011; Cook et al. 2015). This results in a wide array of possible products, including several types of organic

compounds, which could be important for the emergence of life (Bernstein et al. 1999). For example, UV irradiation of anthracene embedded in H_2O can result in anthraquinones, which are of special interest, as quinones are fundamental to biochemistry (Ashbourn et al. 2007; Öberg 2016). Additionally, PAHs embedded in ices could be used to better understand the surface properties of icy moons, as they can function as probes to study the effect of radiation, providing important information for future in situ missions (Baragiola et al. 2008; Barnett et al. 2012).

Due to their possible role in the emergence of life, but also their potential to investigate surface and atmospheric processes, efforts have been made to detect PAHs on solar system bodies. Spectral signatures attributed to PAHs were detected on the surface of Saturn's icy moons Iapetus and Phoebe (Cruikshank et al. 2008), as well as in the upper atmosphere of Titan (López-Puertas et al. 2013). Furthermore, PAHs were detected in carbonaceous chondrites, for example, in the Allende meteorite (Becker & Bunch 1997), the Murchison meteorite (Sabbah et al. 2017), and samples from the comet 81P/Wild 2 (Clemett et al. 2007). Therefore, PAHs were suggested to have been present in the early stages of solar system formation (Plows et al. 2003), possibly contributing to the inventory of materials that formed planetary objects and minor bodies. The PAHs may have been implanted directly on primordial bodies from the planetary accretion disks and/or delivered by comets and meteorites (Allamandola 2011). In addition to being deposited onto surfaces, PAHs could form in situ on planetary surfaces (Zolotov & Shock 1999).

For the reasons stated above, there is significant interest in the detection and analysis of extraterrestrial PAHs through space exploration missions. On the surface of Mars, NASA's Curiosity rover has identified thiophenes, which are similar to PAHs in their structure, consisting of five-membered rings with four carbon atoms and one sulfur atom (Eigenbrode et al. 2018). Furthermore, dichlorobenzene has been identified by Curiosity (Szopa et al. 2020), possibly pointing to organic compounds in the soil. More recently, benzoic acid was detected in a soil sample by Curiosity (Millan et al. 2022). Despite these discoveries, PAHs have not yet been directly detected on the surface of Mars, and it is suggested that the ultraviolet radiation from the Sun destroys them in a time frame of 4–9.6 sols (solar day as measured on Mars) without shielding (Dartnell et al. 2012). The PAHs could be shielded in the south polar residual cap region by the present ice (Campbell et al. 2021) or found in the subsurface soil. Although PAHs are thought to be destroyed over a short time frame on the surface of Mars due to the UV radiation, a number of PAHs could survive under Venus-like conditions, as they form stable solutions in concentrated sulfuric acid, among them perylene (Bains et al. 2021).

One method that is potentially well suited for in situ investigation of PAHs is laser desorption mass spectrometry (LDMS). This is characterized by a high sensitivity and relatively low fragmentation, as well as requiring minimal sample processing, allowing for analysis of the sample with minimized risk of contamination. It has proven to be well suited for detecting PAHs (e.g., Hahn et al. 1987; Faccinetto et al. 2008; Sabbah et al. 2012) and has been used to probe PAH growth within carbonaceous grains (Gavilan Marin et al. 2020) and detect PAHs in carbonaceous chondrite meteorites (Spencer et al. 2008) and meteoritic acid residues (Kovalenko et al. 1992). Because of its sensitivity, LDMS has proven very useful in astrophysical applications. It can be used for the analysis of samples with low concentrations of the analyte, which are often encountered in extraterrestrial material. Landers and rovers already using or planning to use LDMS include the Mars Organic Molecule Analyzer (MOMA) suite on the Rosalind Franklin rover, set to launch in 2022 (Goesmann et al. 2017), and the Dragonfly Mass Spectrometer on board the Dragonfly mission (Grubisic et al. 2021). Both instruments have a demonstrated ability to detect PAHs.

Instruments capable of detecting organics at trace concentrations are crucial for the detection and classification of biotic and/or abiotic organic compounds and will only increase in importance for future in situ space exploration missions. The ORganics Information Gathering INstrument (ORIGIN) system, developed at the University of Bern, is a space prototype instrument for in situ measurements on planetary surfaces. ORIGIN consists of a miniature reflectron-type time-of-flight mass spectrometer (R-TOF), which uses a nanosecond laser system to desorb and ionize surface material in order to analyze the chemical composition of the sample. In a previous study, ORIGIN was shown to be capable of detecting amino acids at concentrations relevant for future in situ space missions (Ligterink et al. 2020).

In this work, we present proof-of-principle measurements showing that ORIGIN is capable of desorbing, ionizing, and detecting PAHs at different concentrations and over a range of applied laser pulse energies. This study, in combination with previous results, shows ORIGIN's potential as an instrument to detect a variety of organics for future in situ space missions.

2. Methods and Instrument

2.1. ORIGIN

ORIGIN is based on LDMS. The instrument is described in detail in Ligterink et al. (2020). In this work, a short description of the instrument is given.

The core of ORIGIN consists of a lightweight and miniature R-TOF (160 mm × Ø 60 mm) mass spectrometer (Rohner et al. 2003) with a mass resolution of $m/\Delta m > 1000$ operated in desorption mode and housed in a vacuum chamber. The vacuum chamber can be opened to introduce the sample holder into the system, which is placed on a translation stage installed below the entrance of the mass spectrometer. The sample holder is made out of stainless steel, and five cavities are located on the surface (0.2 × Ø 3 mm), in which 1 μl of sample solution can be dropcast. The solvent is given time to sublimate, and a film of molecular sample material is left. In Figure 1, the schematic of the sample holder is shown. After sample introduction, the vacuum chamber is evacuated by a turbomolecular pump backed by an oil-free membrane pump. With this system, a typical pressure of 5×10^{-8} mbar can be achieved. Prior to opening, the system is vented with high-purity nitrogen (Alphagas 2, Garbagas) to avoid contamination of the chamber by outside air during the sample exchange. ORIGIN uses a nanosecond pulsed Q-switched Nd:YAG laser ($\lambda = 266$ nm, pulse duration ~3 ns, pulse repetition rate = 20 Hz, focal spot size Ø = ~30 μm) installed outside the vacuum chamber. A beam guiding system is used to guide the laser pulses toward the mass analyzer, passing through a quartz window installed on top of the vacuum chamber. The

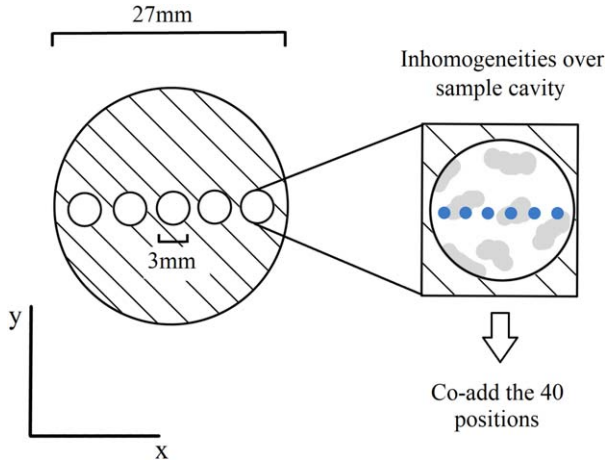

Figure 1. Schematic drawing of the sample holder with its five cavities (left). A zoom of a single cavity (right) shows the analyte inhomogeneities in the sample (gray areas), which have been exaggerated to exemplify the purpose of averaging over the 40 positions. The blue points signify the laser pulses. Note that not all of the 40 positions are shown. The x and y directions for the orientation of the sample stage are indicated. In this sketch, the z direction points out of the plane of the paper.

laser can be operated at different laser pulse energies. During operation, the laser desorbs material located on the sample holder, which are neutral and ionized atoms and molecules of the sample (Wurz et al. 1992). Cations will enter the mass spectrometer, which is located below the laser entrance window. There, the mass-to-charge ratio of the ions is measured and the molecule identified.

For each measurement, a TOF spectrum was recorded at 40 positions, separated by a spacing of approximately 50 μm. Each position was hit with 100 laser shots, resulting in a total of 4000 single spectra. The aim of this measurement procedure is the minimization of error caused by inhomogeneous concentration of the sample material in the cavity.

2.2. Sample Preparation

For this measurement campaign, the following four PAHs are used: anthracene ($C_{14}H_{10}$, Sigma-Aldrich, 99%, $M = 178.2$ g mol^{-1}), pyrene ($C_{16}H_{10}$, Sigma-Aldrich, 98%, $M = 202.3$ g mol^{-1}), coronene ($C_{24}H_{12}$, Sigma-Aldrich, 97%, $M = 300.4$ g mol^{-1}), and perylene ($C_{20}H_{12}$, Sigma-Aldrich, $\geqslant$99%, $M = 252.3$ g mol^{-1}).

All sample preparation steps were performed under laboratory conditions in a sterilized flow hood (ISO5). The PAHs were dissolved in n-heptane (Sigma-Aldrich, 97%). Several stock solutions of various concentrations were prepared for the different PAHs, and the 100 μM is the most commonly used one. For convenience, the concentration of the solution is generally used in this paper to indicate how much material was present during a measurement. However, we note that in each prepared sample, the solvent is sublimated; therefore, strictly speaking, we are no longer dealing with a concentration.

Before dropcasting a sample on the sample holder, a cleaning routine was followed. A beaker was filled with isopropanol and the sample holder placed inside so that it stood upright. The beaker was placed in an ultrasonic bath for 15 minutes. Afterward, the sample holder was washed with Milli-Q grade water (TOC $<$ 5 ppb), after which the sample holder was placed on a heating plate in a flow hood for at least 30 minutes to sublimate the water from its surface. The sample holder and any equipment used in the next steps were flame sterilized by a propane/butane flame at $T > 500$°C. Once the sample holder had cooled down to room temperature, sample material was dropcast into the cavities, and the solvent was left to sublimate before introduction of the sample holder into the vacuum chamber.

2.3. Measurement Procedure

After the sample holder was placed into the vacuum chamber, the system was pumped down to a pressure of $<10^{-7}$ mbar. The laser optics of the system were cleaned with high-purity nitrogen before each experiment to avoid any contamination by dust. The stage on which the sample holder was placed was moved to a point $\sim$1 mm below the entrance of the TOF entrance electrode, which is slightly out of focus of the laser.

Two sets of measurement campaigns were performed in this study to test the instrument's capabilities for detecting PAHs: laser pulse energy scans and concentration scans.

For an energy scan, a position on the sample is irradiated by the laser with a pulse energy of 1 μJ, the next position with 2 μJ, the next with 3 μJ, and a fourth with 4 μJ. This sequence is repeated a total of 10 times, resulting in 40 positions on the sample surface, 10 for each applied pulse energy. Each of the 40 positions is hit with 100 laser shots, which results in a total of 1000 spectra for each applied pulse energy.

For the concentration scan, each cavity contains a sample with a different concentration that is measured at a constant laser pulse energy of 3 μJ for all 40 positions. Past experience has shown that this laser pulse energy yields the best performance and highest signal at a comparatively low risk of saturating the detector (Ligterink et al. 2020). Furthermore, at higher laser pulse energies, more ions are produced, which results in increased Coulomb repulsion in the ion plume and subsequently can lead to broadening of the mass peaks.

2.4. Data Analysis

All data are analyzed using Matlab software developed in-house; see Meyer et al. (2017) for a detailed description. In a first filtering of the data, any spectra that contain a peak with a signal-to-noise ratio (S/N) $\geqslant$ 6 are selected. This filtering step ensures that mass spectra in which no ions were detected are removed from the set. However, any spectrum that has a mass peak, even if it only results from contaminants such as sodium or potassium, is accepted and used for further analysis. On average, three-fourths of the spectra fulfill this criterion. These selected spectra of the 100 laser shots with a desired S/N are coadded to create a single spectrum per position; subsequently, the spectra of the 40 positions are coadded again to a single TOF spectrum to average out the variations due to potential inhomogeneous analyte concentration in a sample cavity. It is possible to analyze all positions individually.

The area of the peaks is calculated with an automated routine in the Matlab software via Simpson integration (Meyer et al. 2017). A baseline subtraction is done for all plots presented in this paper, but the analysis of the spectra was performed on the raw and untreated spectra.

The limit of detection (LOD) is calculated in this study following the notation in Ligterink et al. (2020) by using the

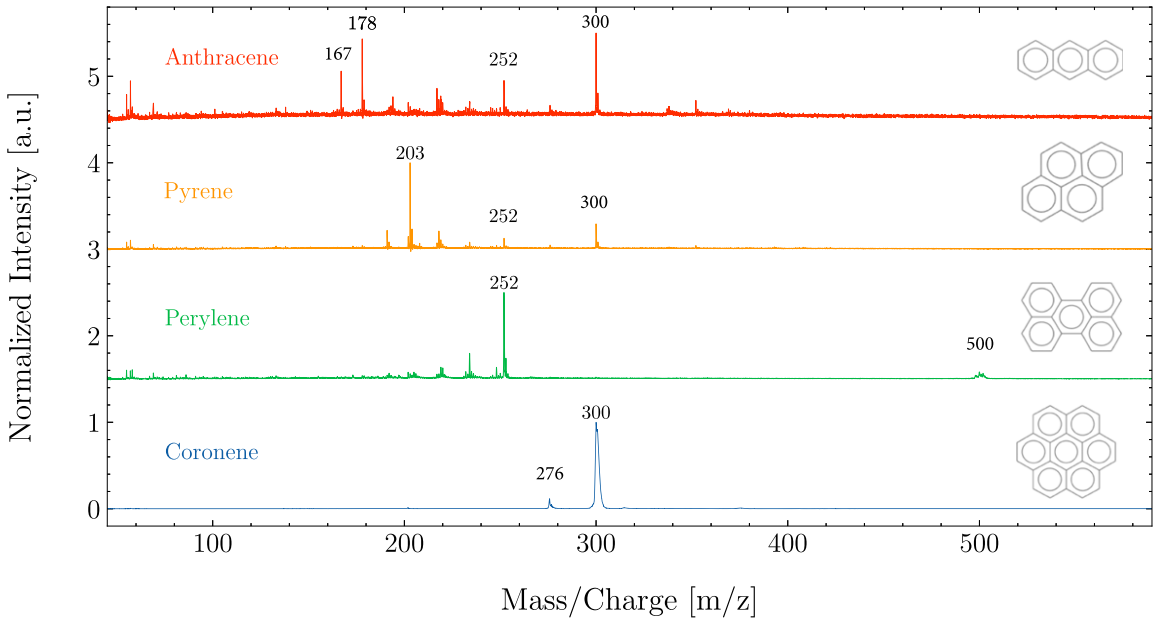

Figure 2. Mass spectra of the four PAH species investigated in this campaign measured at a laser pulse energy of 4 μJ. From bottom to top, the PAHs displayed are coronene ($C_{24}H_{12}$, spectra shown in blue), perylene ($C_{20}H_{12}$, spectra shown in green), pyrene ($C_{16}H_{10}$, spectra shown in orange), and anthracene ($C_{14}H_{10}$, spectra shown in red). A concentration of 100 μM was used for all PAHs in this measurement. Prominent peaks are indicated in the plot. The spectra are normalized to the highest peak for the respective PAH and offset from each other. The structure of the PAHs is shown on the right side.

average surface concentration,

$$C_{\text{surf}} = \frac{V \cdot C}{A}, \tag{1}$$

with V being the dropcast volume in the cavity in liters, C being the concentration of the solution in M (mol l^{-1}), and A being the surface area of the cavity ($\sim$7.068 mm^2), which results in an average surface concentration given in mol mm^{-2}.

In this work, a 3σ limit for detection is used, leading to the following equation for the calculation of the LOD:

$$\text{LOD}_{3\sigma} = \frac{3}{\text{S/N}} \cdot C_{\text{surf}}, \tag{2}$$

where S/N is the S/N of the PAH mass peak investigated, which is calculated by the Matlab software based on the noise determined in a mass peak–free region and the intensity of the peak under investigation.

To quantify the error of the measurements with ORIGIN, the ratios of the most abundant PAH peaks at a certain m/z with respect to the $m/z+1$ peaks were analyzed for pyrene and perylene at the 40 individual scan positions and the mean and standard deviation of the ratio calculated. The peak at $m/z+1$ is assumed to correspond to the main mass with one ^{12}C replaced with a ^{13}C atom. The ratio between the two peaks was estimated in the following way:

$$\frac{Y}{X} = \frac{C \cdot [^{12}\text{C}]^{C-1} \cdot [^{13}\text{C}]}{[^{12}\text{C}]^{C}}, \tag{3}$$

with X and Y being the integrated area of the m/z and $m/z+1$ peaks, respectively; C being the number of carbon atoms in the PAH; and [^{12}C] and [^{13}C] being the abundances of the isotopes. The possibility of the $m/z+1$ peak corresponding to a hydrogen atom replaced by a deuterium atom was considered but deemed to be of negligible probability in this study, compared to the contribution of carbon due to the much lower terrestrial D/H ratio versus that of ^{13}C/^{12}C.

The ratio of the two mass peaks is a function of the number of carbon atoms for a PAH and therefore differs from PAH to PAH due to the number of carbon atoms, but it can be assumed that the respective ratio should remain constant for each of the 40 positions measured for one PAH. An average standard deviation of 20% from the expected ratio is calculated this way and attributed to the variation in laser pulse energy over the course of a measurement. See Appendix B for additional information.

3. Results

The aim of this study was to asses the capabilities of ORIGIN to detect PAHs at different concentrations and laser pulse energies. The spectra in this section begin at $m/z=50$. Lower masses were omitted, as they are dominated by contamination on the sample holder from sodium and potassium, and no significant peaks from the PAHs were identified.

Due to their high number of carbon atoms, the parent peaks and potential fragments of the PAHs in this measurement campaign should be accompanied by peaks corresponding to the natural ^{13}C abundance. Therefore, the ^{13}C/^{12}C ratio is used to help identify potential PAH peaks and distinguish them from residual peaks, as well as rule out alternative compositions, which would result in the measured m/z.

In Figure 2, the normalized mass spectra of all four PAHs are shown for a laser pulse energy of 4 μJ, which is the highest laser pulse energy used in this study.

Anthracene shows the lowest signal intensity, leading to prominent contamination from other PAHs (specifically coronene) showing up more pronounced. The peak at $m/z=167$ is most likely a contamination of the anthracene sample itself. Peaks at $m/z=300$, 252, and 202 are contaminations from the other PAHs used for the measurement campaign.

For pyrene, the $m/z=203$ mass peak has been indicated instead of the parent peak at $m/z=202$. In the case of pyrene,

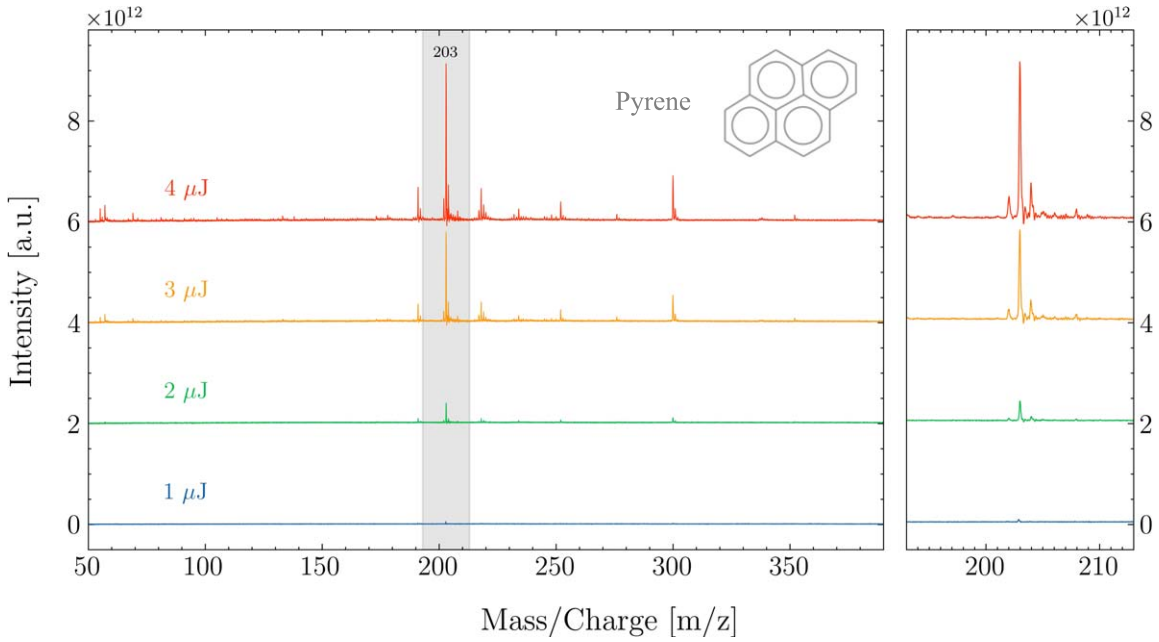

Figure 3. Mass spectra of pyrene, measured at a laser pulse energy of, from bottom to top, 1 (blue), 2 (green), 3 (orange), and 4 (red) μJ and with an average surface concentration of 14 pmol mm^{-2}. A zoom on the area shaded in gray is provided in the right panel. The most abundant peak is indicated with its mass, and the spectra are offset from each other.

$m/z = 203$ is the most abundant peak due to a suspected protonation. This will be discussed in more detail in Section 4. Most peaks besides the $m/z = 203$ peak of pyrene can be attributed to residual PAHs on the sample holder that were not removed by the cleaning routine or peaks from the steel sample holder itself. A mass spectrum of the cleaned steel sample holder without any molecules deposited on it is shown in Appendix A. A peak at $m/z = 191$ could not be attributed to either of these sources of contamination but was determined to most likely be a contamination of the pyrene sample itself.

For perylene, the parent peak at $m/z = 252$ can be clearly observed, as well as multiple peaks around $m/z = 500$.

Coronene shows the highest signal intensity, presumably saturating the detector, which results in peak broadening and thus blending of the $m/z = 300$ and 301 peaks. The only other peak in the mass spectrum can be seen at $m/z = 276$ and attributed to a contamination of the coronene sample by benzo [ghi]perylene, which is a known impurity of coronene (Bréchignac et al. 2005). This sensitivity of ORIGIN toward coronene allows for trace amounts of it to be detected as contamination in other samples. Therefore, the coronene peak is still observed for the anthracene and pyrene samples. Although the system shows high sensitivity to PAHs, ORIGIN is not able to distinguish between isomers directly. Previous results in Ligterink et al. (2020) have shown that the fragmentation patterns of amino acids can differ between isomers and therefore allow for the identification of the parent isomer. As fragmentation in the tested selection of PAHs is limited, such isomer identification by fragmentation pattern is unlikely to work for PAHs. Nevertheless, it is possible that a different laser wavelength could be used to induce fragmentation, which might allow the subsequent identification of the isomer.

3.1. Energy Scan

For the energy scans, a constant concentration of 100 μM was used for each PAH sample, corresponding to a surface concentration of 14 picomol mm^{-2}. Figure 3 shows the mass spectra of an energy scan performed on pyrene. Similar plots for the other three PAHs can be found in Appendix A. The most abundant peak at $m/z = 203$ is clearly visible and increases in intensity as a function of the laser pulse energy. The peaks at $m/z = 300$ and 252 can be attributed to coronene and perylene, respectively, whereas the peak at $m/z = 191$ is most likely a contamination in the pyrene sample. The peak cluster around $m/z = 220$ is a known contamination from the steel sample holder; see Appendix A.

In Figure 4, the peak area of the parent mass of each PAH is presented and normalized to the value at 4 μJ. The increase in

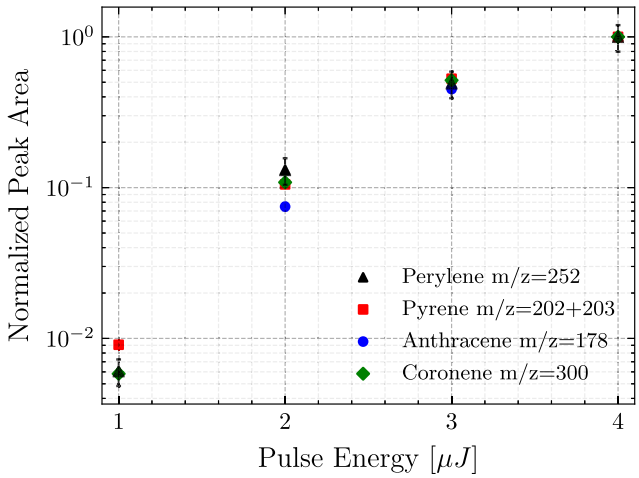

Figure 4. Normalized peak area of the parent peak for the four PAHs as a function of applied laser pulse energy. Displayed are perylene (black triangle), pyrene (red square), anthracene (blue circle), and coronene (green diamond). The standard error of 20% as explained in Section 2.4 has been added to the perylene measurement to indicate the magnitude and omitted from the other measurements for easier readability of the plot. Note that there has been no detection of a peak for anthracene at 1 μJ.

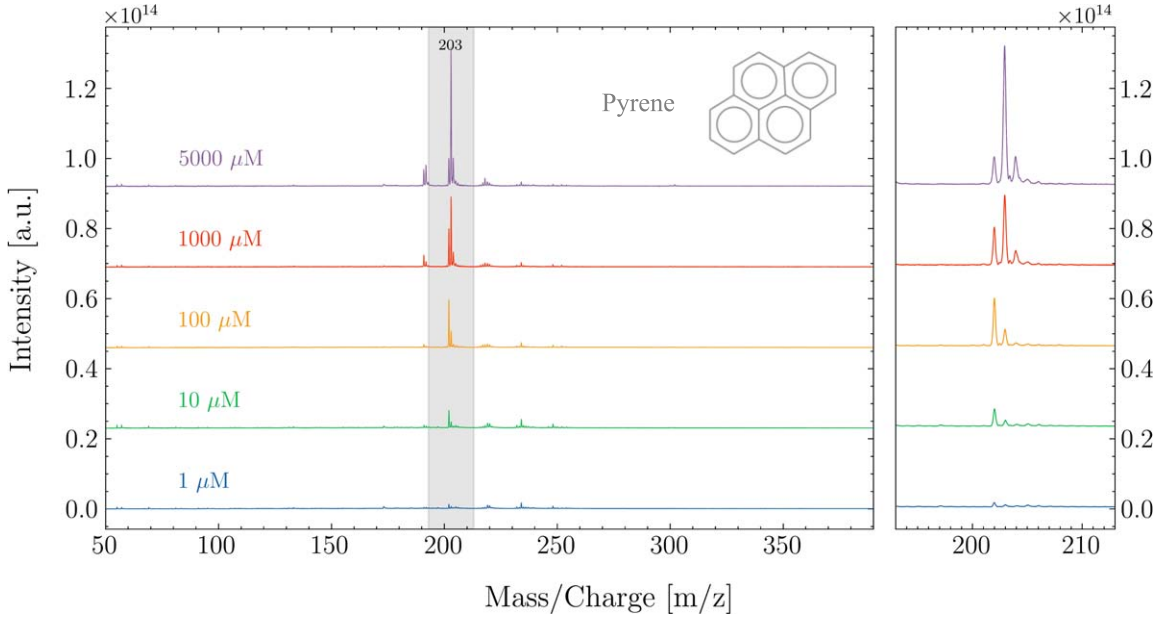

Figure 5. Mass spectra of pyrene for a series of concentrations measured at a fixed laser pulse energy of 3 μJ. From bottom to top, the concentrations are 1 (blue), 10 (green), 100 (orange), 1000 (red), and 5000 (purple) μM. A zoom on the area shaded in gray is provided in the right panel. A clear transition from the parent peak at $m/z = 202$ for low concentrations to $m/z = 203$ for high concentrations is visible. The structure is shown in the top right corner of the left panel, and the spectra are offset from each other.

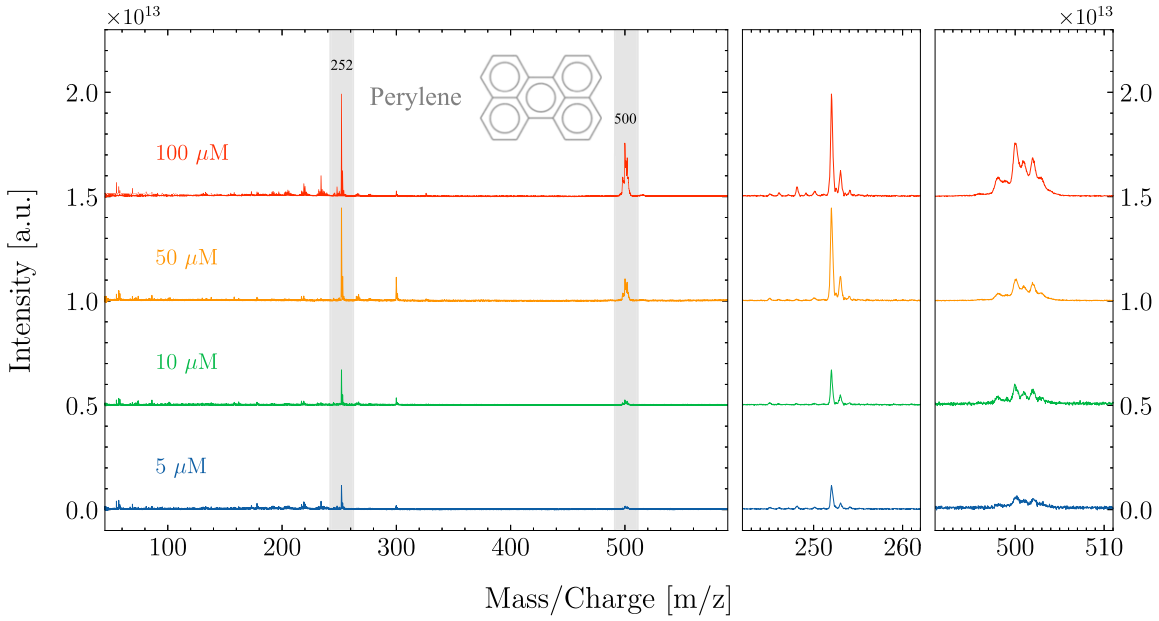

Figure 6. Concentration scan measured for perylene at a laser pulse energy of 3 μJ. From bottom to top, the concentrations used are 5 (blue), 10 (green), 50 (orange), and 100 (red) μM. The areas shaded in gray in the left panel are shown in the right panels, providing a zoom on the parent peak of perylene at $m/z = 252$ and on the masses around $m/z = 500$. To see the structure of the masses around $m/z = 500$, the data for 5 and 10 μM are multiplied by a factor of 4 in the right panel. The structure of perylene is shown in the left panel, and the spectra are offset from each other.

signal intensity for the parent peaks as a function of laser pulse energy is clearly visible, and all four PAHs follow the same trend. For pyrene, the peak areas for $m/z = 202$ and 203 are summed to account for the parent mass and its chemical derivative, which is most likely due to a suspected protonation.

3.2. Concentration Scan

Concentration scans have been performed on pyrene, perylene, and anthracene. The concentration scans for pyrene and perylene are shown in Figures 5 and 6, respectively. A similar plot for anthracene is shown in Appendix A. In the pyrene sample, a shift from the most abundant peak at the parent mass $m/z = 202$ to 203 is observed as the surface concentration of the PAH increases.

In Figure 6, the increase of intensity of the parent peak $m/z = 252$ as a function of the concentration can be observed for perylene, as well as the emergence and increase in intensity of masses around $m/z = 500$, which will subsequently be called

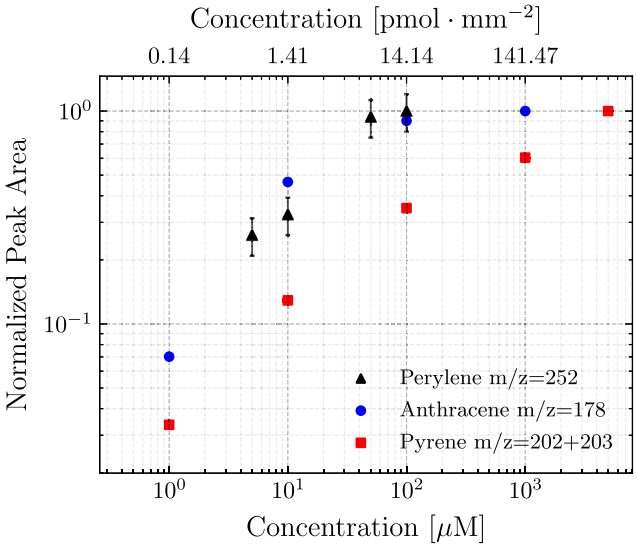

Figure 7. Normalized peak area for the PAHs as a function of concentration. The PAHs shown are perylene (black triangle), anthracene (blue circle), and pyrene (red square). The error bar has been added for perylene to exemplify the magnitude of the error and has been omitted from the other PAHs for clarity.

the dimer cluster, though it is most likely the result of a combination of the perylene parent and a chemical derivative of the parent. At such high masses and at the settings applied to the ion optical system of the mass analyzer in this study, the resolution of the system is no longer sufficient to clearly resolve the masses. In addition to the parent peak at $m/z = 252$, three peaks can be seen at $m/z = 250$, 248, and 246. This could be the result of hydrogen loss, corresponding to -2H, -4H, and -6H, respectively, from the parent molecule. Such a pattern of hydrogen loss has been observed for PAHs in previous work (Castellanos et al. 2018). Similarly, multiple peaks around $m/z = 500$ can be observed, though they can no longer be clearly resolved due to the aforementioned mass resolution decreasing for high masses. The most prominent peaks correspond to $m/z = 498$, 500, and 502. Perylene is the only PAH used for which this dissociation pattern is observed.

Figure 7 shows the increase of the peak areas for the parent peak of the PAHs as a function of concentration. The intensities are normalized to the highest value for each set of measurements. For anthracene, the intensity increases rapidly as a function of concentration, but appears to flatten out at concentrations above 100 μM. For perylene a similar behavior is observed, which is most likely linked to the emergence of the dimer cluster at around $m/z = 500$. For pyrene, a similar trend can be observed, but the trend appears to be shifted to higher concentrations compared to anthracene and perylene.

We note that at the settings used for the experiments, the flattening of the curve for larger concentrations is due to neither overranging during the acquisition of the data nor saturation of the detector.

3.3. Limit of Detection

The LOD has been calculated for the energy and concentration scans using Equation (2), and the result is shown in Figure 8. A lower LOD means that a smaller amount of the substance can be detected. For the concentration scan, an increase in the LOD can be observed as a function of concentration, whereas for the energy scan, the LOD decreases as the pulse energy increases.

For anthracene, the highest LOD was calculated in both the energy and concentration scans. Coronene shows the highest sensitivity for detection in the case of an energy scan of around $\sim$10 fmol mm^{-2}, whereas the pyrene masses have the lowest LOD in the concentration scan at $\sim$3 fmol mm^{-2}. For perylene, the lowest value was calculated as $\sim$18 fmol mm^{-2} in the concentration scan.

4. Discussion

In this work, we show that ORIGIN is able to detect PAHs at low concentrations ($<$1.41 pmol mm^{-2}) and laser pulse energies (2–4 μJ). With the LOD$_{3\sigma}$ being on the order of a few fmol mm^{-2} for the majority of the measurements, the instrument demonstrates sensitivity equal to or larger than the linear ion trap analyzer that is part of the MOMA suite on ESA's Rosalind Franklin rover, which reports a sensitivity of LOD$_{3\sigma} \leqslant 1$ pmol mm^{-2} (Goesmann et al. 2017). It must be noted that the sensitivity of ORIGIN can still be increased by increasing the voltages over the MCP detector stack (Riedo et al. 2017) or by increasing the number of positions sampled in a measurement, with an anticipated increase in the sensitivity to sub-fmol mm^{-2}. Every additional $\sim$50 V on the MCP stack increases the sensitivity by a factor of $\sim$2. Previous experiments on amino acids (see Ligterink et al. 2020) were performed at a higher voltage applied over the detector of 2050 V, as opposed to the 1900 V used for this measurement campaign, meaning the sensitivity is decreased by a factor of $\sim$8 compared to the measurements of the amino acids.

At the laser pulse energies used, ORIGIN desorbs and ionizes the sample material without inducing extensive fragmentation or chemical processing that would result in cations, although anions or uncharged fragments, which cannot be detected by the system, may be formed. Therefore, despite also detecting trace amounts of other PAHs due to its sensitivity, the PAHs investigated by ORIGIN can be clearly identified by their parent peaks. This observation of limited fragmentation is in accordance with other recent studies utilizing LDMS to investigate PAHs, such as Gavilan Marin et al. (2020). The majority of other peaks in the spectrum can be attributed to contaminants in the steel sample holder. There is work in progress at the moment to minimize these contributions using different sample holder substrates.

An issue for large molecules in a real-life environment is isobaric interference. In this case, molecules with a different chemical formula but the same nominal mass contribute to the signal at the corresponding m/z and cannot be distinguished from each other at ORIGIN's mass resolving power. This poses a potential issue for natural sample analysis and requires more advanced analytical methods, such as mass spectrometric pattern fitting or additional filtering of natural sample material, to be resolved.

Perylene is the only PAH investigated for which a potential hydrogen loss from the parent molecule is observed in both the concentration and energy scan. This could give an explanation for the dimer cluster after $m/z > 498$, as the reactive $C_{20}H_{10}$, $C_{20}H_8$, and $C_{20}H_6$ radicals could recombine with the parent molecule perylene ($C_{20}H_{12}$), forming the masses $m/z = 502$, 500, and 498, respectively. The additional mass peaks at $m/z = 499$, 501, and 503 correspond to the natural ^{13}C ratio of the resulting molecules.

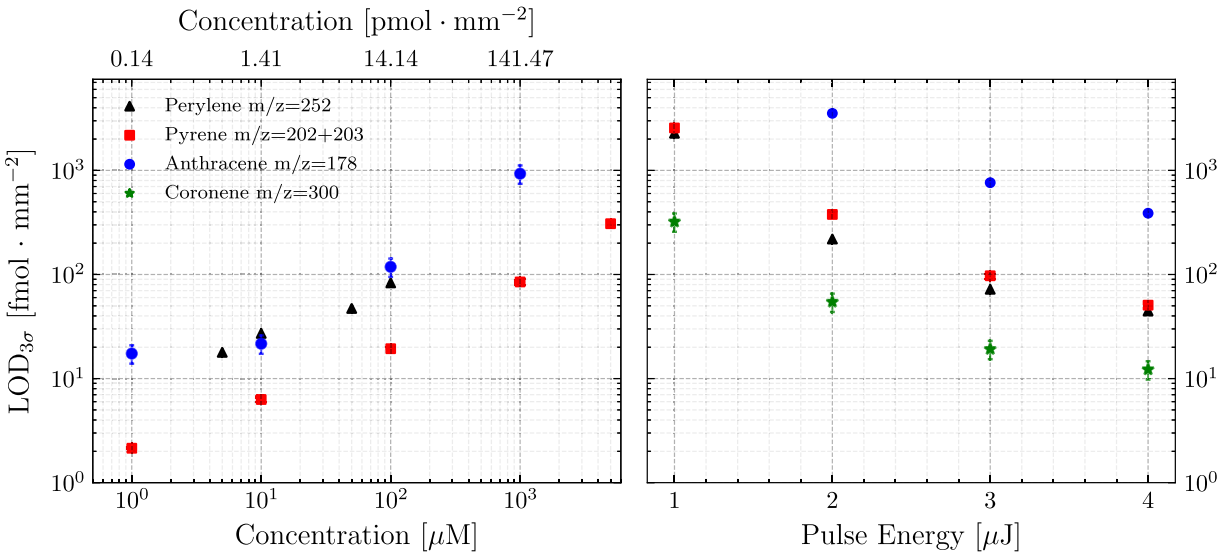

Figure 8. The LOD for the different PAHs calculated as a function of concentration at a fixed applied pulse energy of 3 μJ (left) and of pulse energy using a fixed concentration of 100 μM (right). The PAHs shown are perylene (black triangle), pyrene (red square), anthracene (blue circle), and coronene (green star). The error bar has been added for one PAH in both plots to show the magnitude of the error and has been omitted from the other measurements for readability of the plot. It should be noted that for anthracene, no peak has been detected at $m/z = 178$ for a laser energy of 1 μJ.

The change in the most abundant mass peak for pyrene from $m/z = 202$ to 203 for increasing concentration, as seen in Figure 5, is most likely due to protonation of pyrene. For protonation to occur, H atoms need to be available. There are several potential sources for H atoms, such as pyrene itself and steel surface contaminants. Another possible explanation for this phenomenon is the presence of residual n-heptane solvent. Measurements of pure n-heptane have been taken but did not show any mass fragment that could be assigned to this molecule. We therefore assume that n-heptane has fully sublimated from the surface. However, as the concentrations of PAHs increase, a fraction of n-heptane could be trapped in the solid material and act as a proton donor, leading to the protonation of pyrene. To determine the precise cause of this effect and why it is only observed for pyrene, further study is needed but beyond the scope of this work. However, in complex samples found on planetary objects, more molecules that can act as a proton donor could be available; therefore, protonation in pyrene and perhaps other PAHs is expected to be a noticeable effect.

ORIGIN is very sensitive to coronene, which appears to be easily ionized; therefore, even trace amounts on other samples due to cross-contamination are detected with a high intensity, such as is the case for the measurements of anthracene. The peak broadening seen in Figure 2 can be attributed in part to this sensitivity, as this measurement most likely saturates the detector system. Additionally, there could be repulsion within the coronene ion plume from the large number of charged particles, which therefore results in the peak broadening due to Coulomb repulsion.

The apparent flattening of the peak area as a function of pulse energy, seen in Figure 4, could be due to nearing the energy at which ablation would happen on the surface of the sample or because there is no longer any material on the surface to desorb. Figure 7 shows the peak area as a function of concentration. The peak areas of perylene and anthracene appear to flatten out after a certain concentration. The peak areas for pyrene follow the same trend, but the curve appears to be shifted toward higher concentrations. As seen in Figure 5, the protonated peak becomes dominant above a certain concentration, whereas the parent peak decreases in intensity, most likely resulting in this apparent shift toward higher concentrations for pyrene. It is likely that for even higher concentrations, the peak area would follow a similar trend to the parent peaks of anthracene and perylene and flatten out. This trend could be due to the fact that after a certain concentration, the surface of the sample holder is covered by sample material, so that despite increasing the concentration further, a similar amount is released by laser pulses of the same energy from the top layer.

In Figure 6, the mass around $m/z = 500$ for perylene increases as a function of concentration. The result indicates that for higher concentrations, more hydrogen loss is observed due to more available perylene, the fragments of which then recombine with perylene to form the dimer cluster around $m/z = 500$.

For anthracene, the lowest signal intensity was recorded, but the PAH can still be clearly identified by the parent peak at $m/z = 178$ in both the energy (>2 μJ) and concentration scans. The low signal intensity could be due to the interaction of the laser with the molecule not resulting in an efficient production of cations.

The absorption spectra in the UV of pyrene, perylene, and anthracene are shown in Figure 9. These spectra are obtained from the PhotochemCAD database (Du et al. 1998; Dixon et al. 2005). The data for coronene were taken from Ehrenfreund et al. (1992). For these data sets, the PAH spectra have been recorded as a solution in cyclohexane. The presented spectra most likely differ from the solid-state ones and should only be treated as a preliminary indication of the interaction of the laser with the respective PAH.

The absorption spectra in Figure 9 show that pyrene has the highest absorption cross section at the wavelength of the laser, followed by perylene, coronene, and anthracene with the lowest absorption. The absorption spectra are in reasonable agreement with our observations of anthracene having the lowest signal, but no large difference in the absorption cross section is observed between the PAHs at the wavelength used.

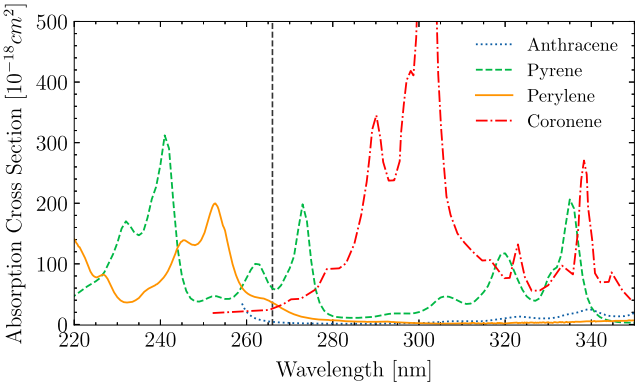

Figure 9. Absorption spectra in the UV of anthracene (blue dotted), pyrene (green dashed), perylene (orange solid), and coronene (red dashed–dotted) recorded as a solution in cyclohexane. The wavelength of the laser (266 nm) used in this measurement campaign is indicated by a gray dashed line. The spectra of perylene, anthracene, and pyrene have been retrieved from the PhotochemCAD database and the data for the spectrum of coronene as a solution in cyclohexane from Ehrenfreund et al. (1992).

Furthermore, the comparatively low absorption cross section of coronene does not match with the observation that it has the highest signal in our measurements. It must be noted that in addition to absorption, effects such as the desorption process and the subsequent postionization, as well as molecule stability, affect the signal strength as well. At present, it remains inconclusive if and how UV absorption influences the laser desorption and ionization process of PAHs with ORIGIN.

5. Conclusion and Outlook

ORIGIN has shown the capability not only of measuring the selected representative PAHs but also of detecting them with higher sensitivity compared to other LDMS-based space instruments while being compact in size. We further show in this work that the chemical processing by ORIGIN and subsequent fragmentation that results in cations of PAHs is negligible at the concentrations and pulse energies used. It is possible that fragmentation would result in negative or neutral ions that are not detected by the instrument, but the parent peaks of the PAHs are still readily detected by the instrument.

The results of this study are a promising indication that other PAHs can be detected with ORIGIN at similar performance. The ORIGIN instrument shows high sensitivity to molecules with aromatic structures because of their strong electronic transitions that aid the desorption (multiphoton) ionization process.

The moons of the giant solar system planets have been chosen as one of the top three priorities for future missions of ESA as part of Voyage 2050, including studies with a lander. ORIGIN would be well suited to investigate the molecular compositions of any of the surfaces of the icy moons, for example, in the context of a lander targeting Europa or Enceladus. Organic material in the near-surface ice on the icy moons, perhaps transported from interior water reservoirs to the surface by vents or plumes, could provide clues to the internal and surface chemical and physical processes of these objects and possibly point to extant life or the necessary conditions for it in the subsurface oceans. Even though ORIGIN has been designed for the purpose of surface analysis, the instrument could also be used in a mission to investigate the presence of PAHs and other molecules with potential biological relevance in planetary atmospheres. A suitable target is Titan, where PAHs have been detected in the upper atmosphere (López-Puertas et al. 2013), or one could search for them in the atmosphere of Venus, where they might survive the sulfuric acid environment (Bains et al. 2021). In this case, haze, droplets, or other particulates in the atmosphere would have to be collected and introduced into ORIGIN for chemical analysis.

In order to investigate planetary surfaces or atmospheres with ORIGIN, an instrument suite would have to be designed that is optimized according to the requirements for the payload depending on the mission. Experience from previous LIMS instruments and designs, such as the LAZMA instrument (Managadze et al. 2011) for the Phobos-Grunt mission, can be leveraged. Payloads that combine an ORIGIN-like laser ablation mass spectrometer with a microscope camera system have been demonstrated (Tulej et al. 2014) and can serve as a basis for future designs. A lightweight miniature laser system, such as a microchip laser, could be utilized in the instrument suite and was tested in combination with laser mass spectrometers in-house for a potential Mercury lander (Riedo et al. 2013). Furthermore, previous experience with mass analyzers can be drawn from the ROSINA instrument on the ROSETTA comet mission (Balsiger et al. 2007) or the NIM instrument for ESA's upcoming JUICE mission to the Jupiter environment (Föhn et al. 2021).

The possibility of sensitively detecting PAHs using ORIGIN, in combination with previous work done on amino acids, highlights its possible use in a future lander mission to detect a wide array of organics. ORIGIN could therefore give valuable insights in the search for biomolecules or their precursors in upcoming space missions.

This work is supported by the Swiss National Science Foundation (SNSF), including Ambizione grant 193453, and NCCR PlanetS. The authors thank H. Linnartz for making the PAH samples available. The authors thank the reviewers for constructive and valuable feedback.

Appendix A
Spectra

In this section, spectra of measurements are collected that have not been included in the main text.

Figure 10 shows the peaks for the clean steel sample holder used in the measurement campaign before any measurements with the PAHs. This figure shows the spectra from $m/z = 5$ on, exemplifying the reason why we omit the lower masses. The two peaks at the beginning of the mass spectrum at $m/z = 23$ and 39 correspond to sodium and potassium, respectively, which are trace elements but readily ionized and therefore appear in the spectrum at a high intensity.

Figure 11 shows two measurements of the steel sample holder: a blank cavity and a cavity in which heptane was deposited. The comparison of the two spectra shows no obvious heptane peaks, but contamination from a pyrene and perylene mixture is apparent.

Figures 12–14 show the intensity as a function of laser pulse energy for anthracene, coronene, and perylene.

The normalized intensity of all four PAHs can be seen measured at a laser pulse energy of 1 μJ in Figure 15. This shows that the peaks of pyrene, perylene, and coronene can be distinguished from the noise even at the lowest laser pulse energy. For the parent peak of anthracene, this is not possible, but the predicted location of the parent peak is indicated in the plot. In

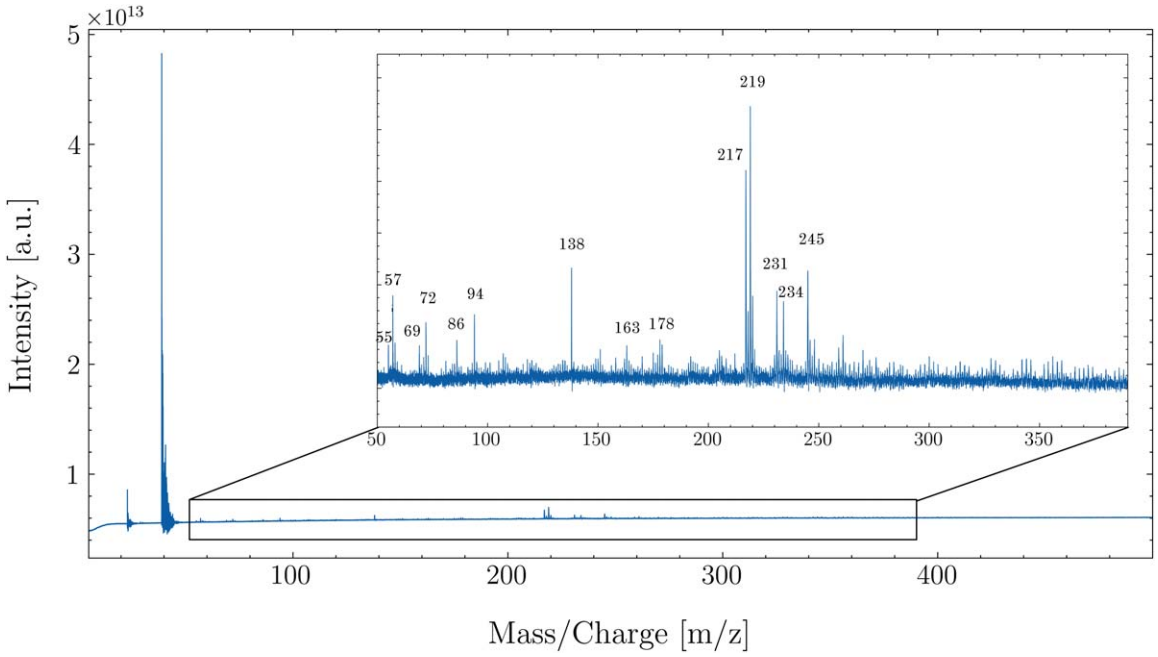

Figure 10. Mass spectrum of the pure steel sample holder starting at $m/z = 5$. The inset shows a zoom from $m/z = 50$ to 390. Typical steel peaks in the relevant mass range are indicated in the spectra. The spectrum was measured at 3 μJ.

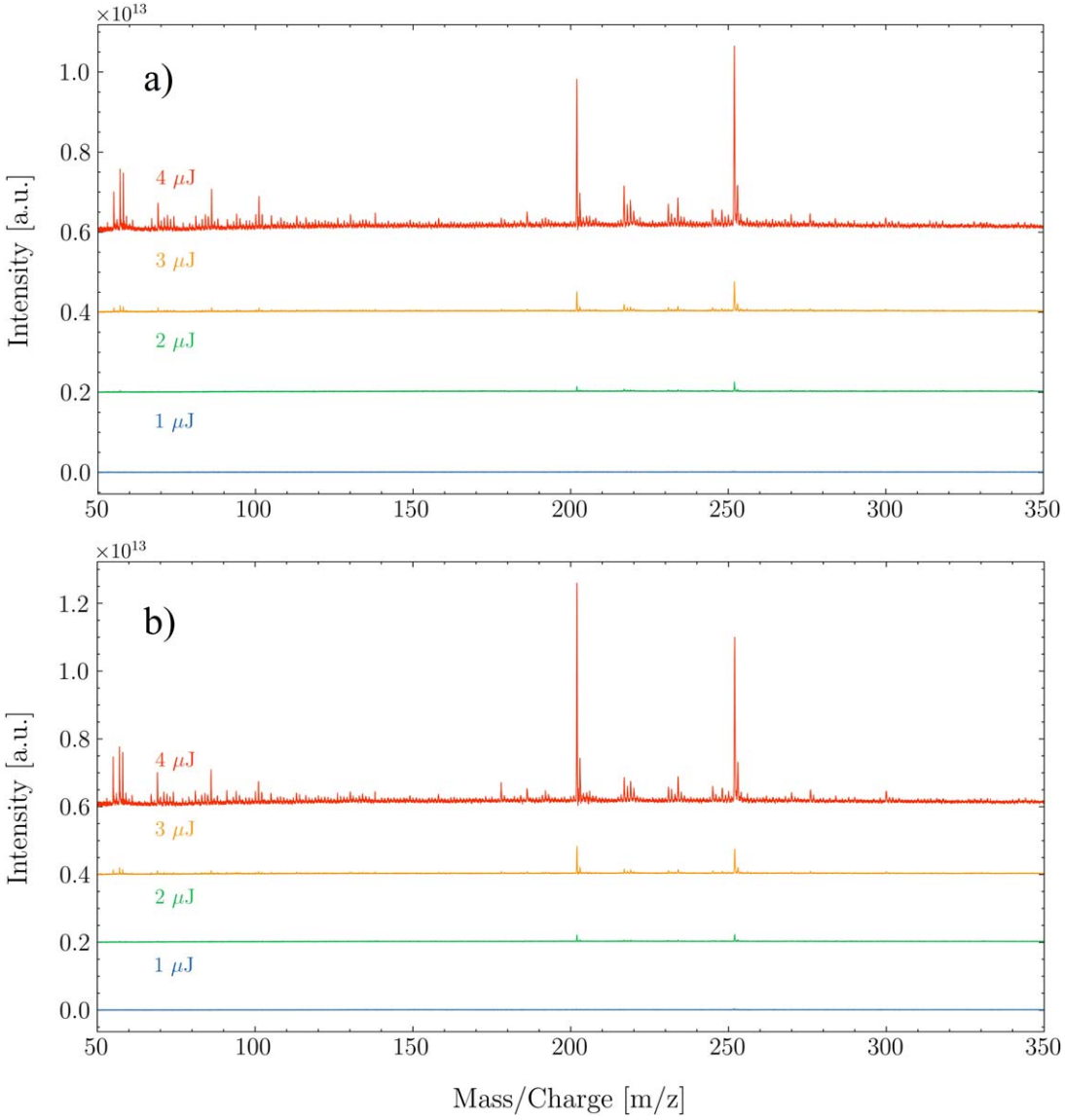

Figure 11. Mass spectra of the blank steel sample holder (a) and heptane deposited on the blank steel sample holder (b), measured at laser pulse energies in the range of 1–4 μJ. Contamination from pyrene and perylene is visible, as a mixture of these two was measured in the adjacent cavities; see Figure 17. No obvious heptane peaks or derivatives could be distinguished in the comparison of the two spectra.

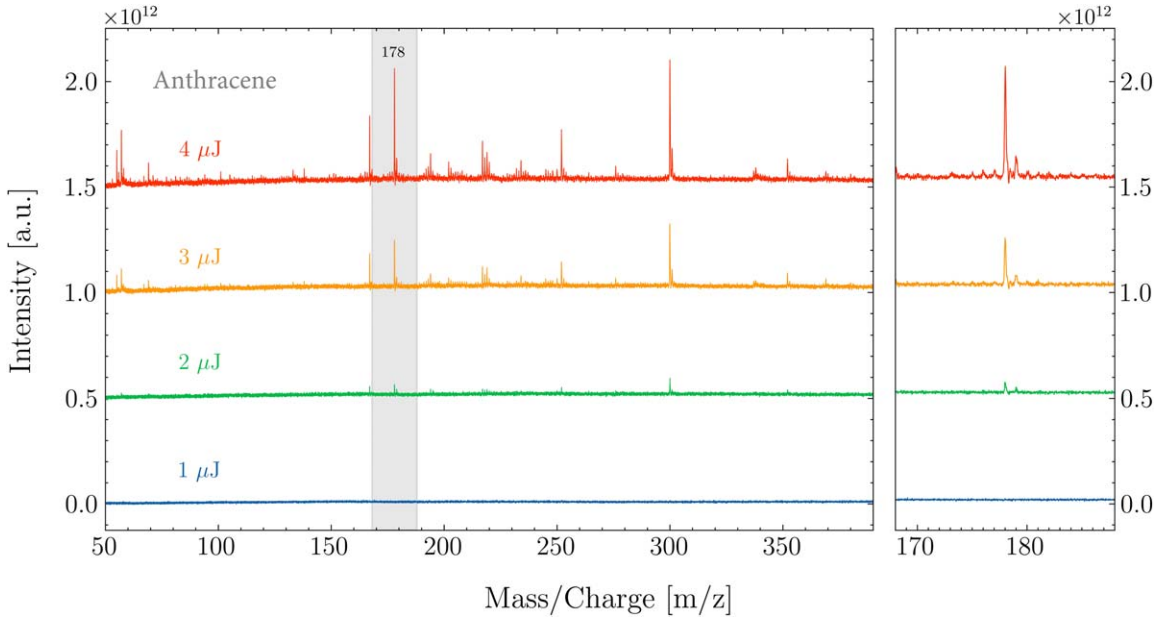

Figure 12. Measurement of 100 μM anthracene at laser pulse energies in the range of 1–4 μJ. The parent peak is indicated in gray.

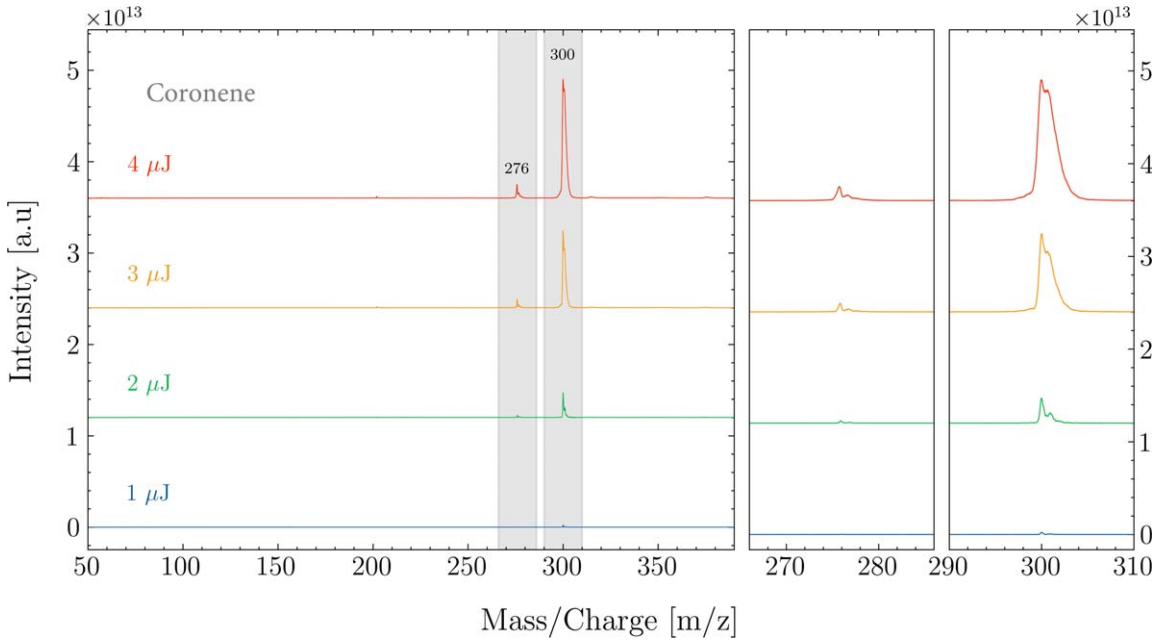

Figure 13. Mass spectra of 100 μM coronene measured at laser pulse energies in the range of 1–4 μJ. The parent peak is indicated at $m/z = 300$, as is the peak at $m/z = 276$.

Figure 16, the intensity as a function of concentration is shown for anthracene. Figure 17 shows the result of a perylene:pyrene and an anthracene:perylene:pyrene:coronene mixture measured with ORIGIN. These measurements were performed in order to assess ORIGIN's performance in analyzing a PAH mixture. For the mixtures, the PAHs were mixed using a 100 μM stock solution of the respective PAHs, and 1 μl of the mixture was dropcast into a cavity. This led to a concentration of 50 μM for each PAH in the case of the perylene:pyrene mixture and 25 μM in the case of the four-component mixture. Pyrene, perylene, and coronene could still be clearly identified via their main mass peaks in the complex four-component mixture, whereas the peak for anthracene could not be clearly identified, most likely due to the strong signal of the other PAHs masking it.

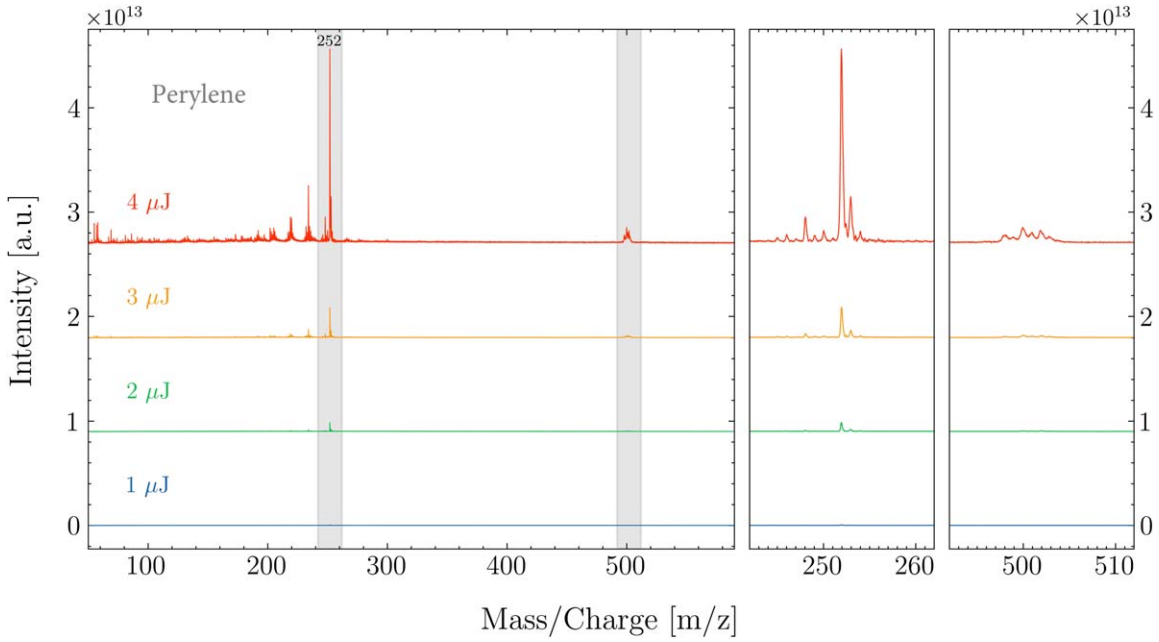

Figure 14. Mass spectra of 100 μM perylene measured at laser pulse energies in the range of 1–4 μJ. The parent peak is indicated.

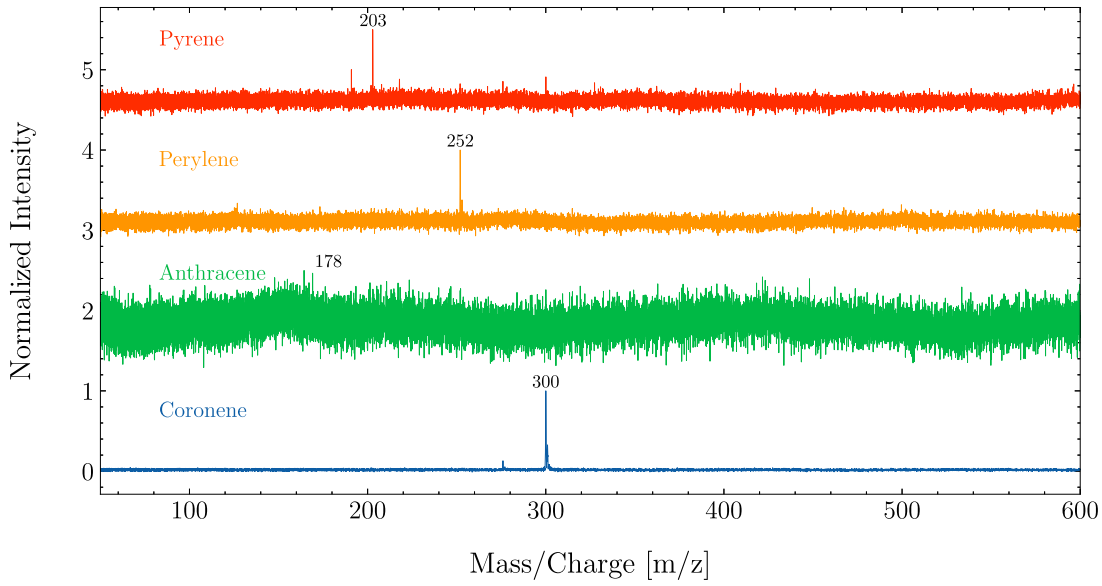

Figure 15. Overview of the four PAHs investigated in this campaign measured at a laser pulse energy of 1 μJ and a concentration of 100 μM. The spectra were normalized to the highest peak for the respective PAH.

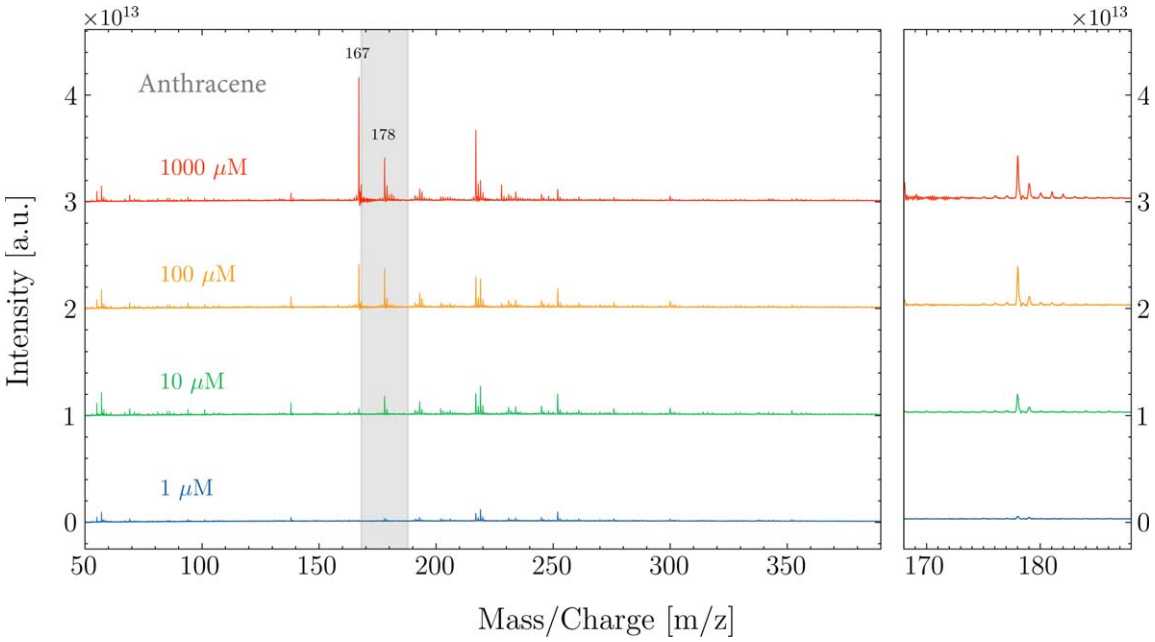

Figure 16. Mass spectra of anthracene at concentrations in the range from 1 to 1000 μM. The sample was measured at a laser pulse energy of 3 μJ.

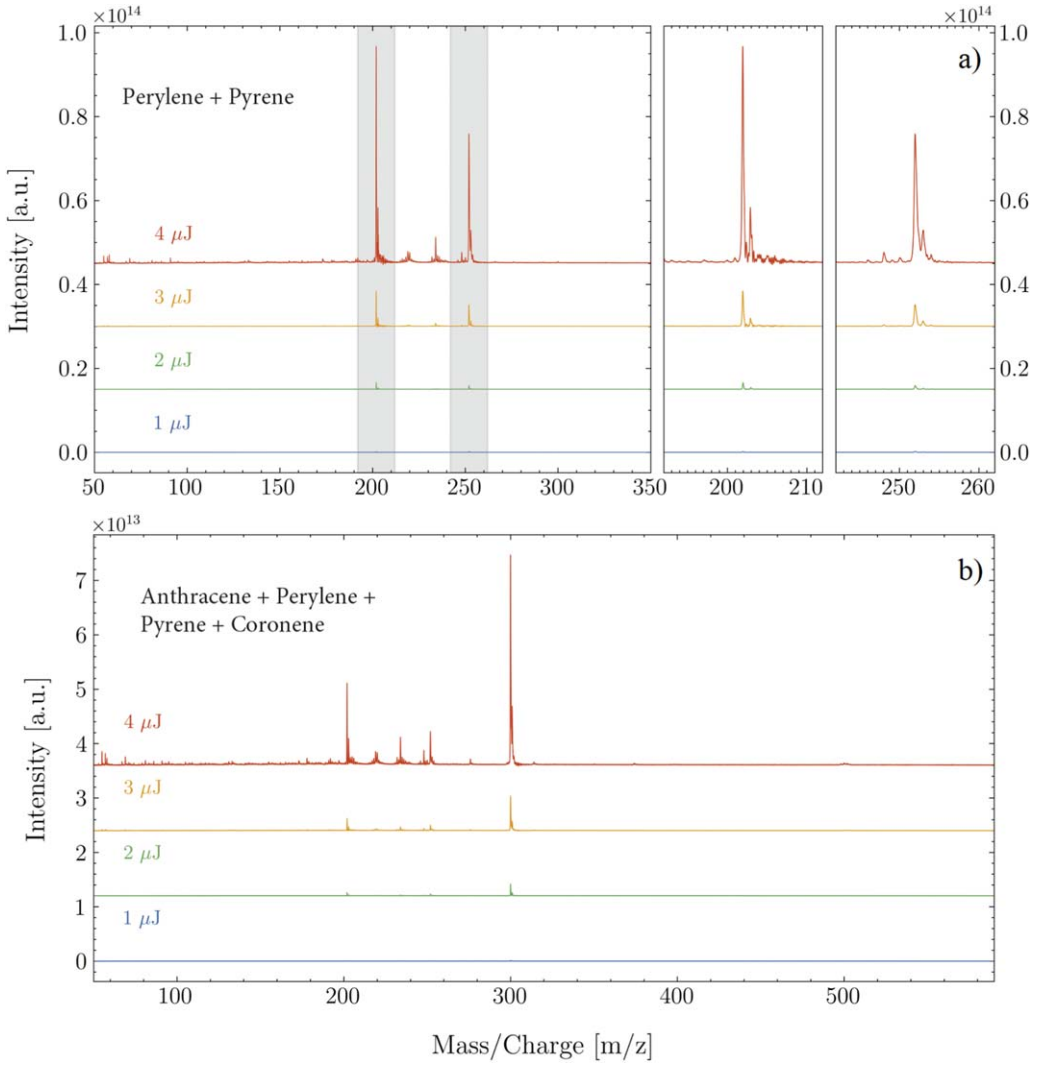

Figure 17. Two PAH mixtures measured with ORIGIN. (a) Perylene and pyrene mixed together with concentrations of 50 μM each. (b) Four-way mixture of all PAHs used in this study. The PAHs mixed together had a concentration of 25 μM each.

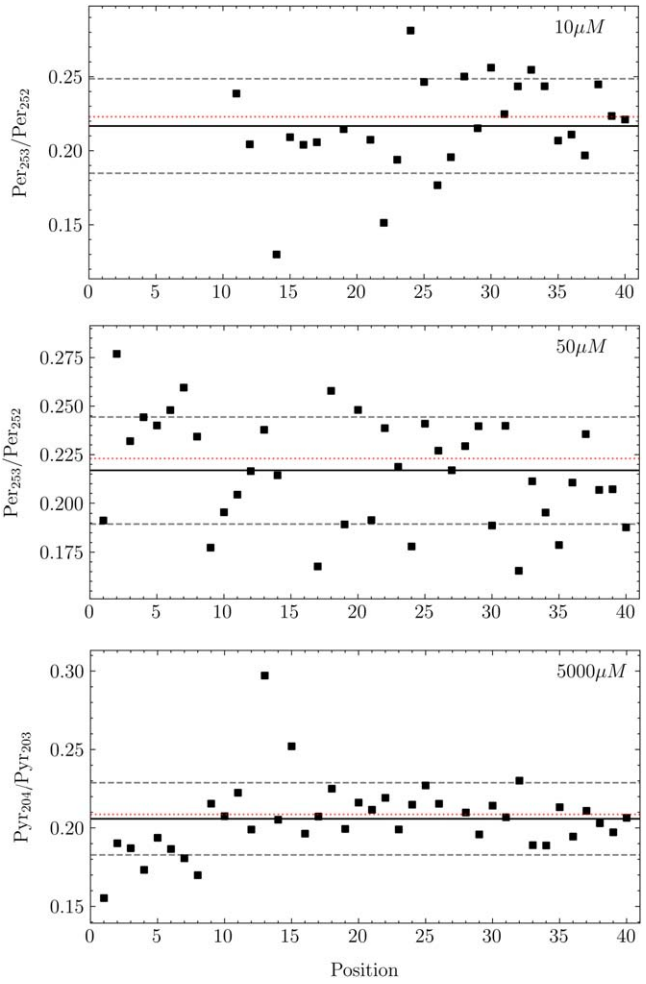

Figure 18. Ratio of the peak area of an $m+1$ mass peak to the peak area with mass m for perylene (abbreviated as Per) and pyrene (Pyr) for the 40 individual positions. The concentration of the investigated sample is shown in the top right corner. The expected ^{13}C ratio (red dotted line) was plotted against the mean of the 40 positions (solid black line) and the standard deviation from the mean (dashed gray lines).

Appendix B
Error Calculation

The plots displayed in Figure 18 show how the error is calculated. For this purpose, the positions out of the 40 individual measurements that have an $S/N > 6$ have been analyzed, and the ratio between the integrated area of the parent peak and its neighboring peak has been calculated. The reasoning behind this is that the ratio should remain constant, as the neighboring peak originates from the natural ^{13}C abundance. The expected ^{13}C ratio has been plotted in the figure as a red dotted line, and the $\pm\sigma$ limit from the mean ratio has been plotted as dashed lines. The error has been derived from the σ limit and determined to be on the order of 20%, which could be attributed to the fluctuation in the laser pulse energy over the course of the experiment and will be considered as the error for all measurements.

ORCID iDs

K. A. Kipfer https://orcid.org/0000-0002-6544-9824
N. F. W. Ligterink https://orcid.org/0000-0002-8385-9149
J. Bouwman https://orcid.org/0000-0002-3615-1703
V. Grimaudo https://orcid.org/0000-0002-7010-5903
C. P. de Koning https://orcid.org/0000-0002-2540-7689
N. J. Boeren https://orcid.org/0000-0001-6162-6953
P. Keresztes Schmidt https://orcid.org/0000-0002-4519-8861
R. Lukmanov https://orcid.org/0000-0001-9257-7410
P. Wurz https://orcid.org/0000-0002-2603-1169
A. Riedo https://orcid.org/0000-0001-9007-5791

References

Allamandola, L. J. 2011, in EAS Publications Ser. 46, PAHs and the Universe: A Symposium to Celebrate the 25th Anniversary of the PAH Hypothesis (Les Ulis: EDP Sciences), 305
Allamandola, L. J., Tielens, A. G. G. M., & Barker, J. R. 1985, ApJL, 290, L25
Ashbourn, S., Elsila, J., Dworkin, J., et al. 2007, M&PS, 42, 2035
Bains, W., Petkowski, J. J., Zhan, Z., & Seager, S. 2021, Life, 11, 400
Balsiger, H., Altwegg, K., Bochsler, P., et al. 2007, SSRv, 128, 745
Baragiola, R., Famá, M., Loeffler, M., Raut, U., & Shi, J. 2008, NIMPB, 266, 3057
Barnett, I., Lignell, A., & Gudipati, M. 2012, ApJ, 747, 13
Becker, L., & Bunch, T. 1997, M&PS, 32, 479
Bernstein, M., Elsila, J., Dworkin, J., et al. 2002, ApJ, 576, 1115
Bernstein, M. P., Sandford, S. A., Allamandola, L. J., et al. 1999, Sci, 283, 1135
Bouwman, J., Boersma, C., Bulak, M., et al. 2020, A&A, 636, A57
Bouwman, J., Cuppen, H. M., Bakker, A., Allamandola, L. J., & Linnartz, H. 2010, A&A, 511, A33
Bouwman, J., Cuppen, H. M., Steglich, M., Allamandola, L. J., & Linnartz, H. 2011, A&A, 529, A46
Bouwman, J., Linnartz, H., & Tielens, A. G. G. M. 2021, JMoSp, 378, 111458
Bréchignac, P., Schmidt, M., Masson, A., et al. 2005, A&A, 442, 239
Campbell, J. D., Schmitt, B., Brissaud, O., & Muller, J.-P. 2021, JGRE, 126, e2020JE006595
Castellanos, P., Candian, A., Zhen, J., Linnartz, H., & Tielens, A. G. G. M. 2018, A&A, 616, A166
Cherchneff, I. 2011, in EAS Publications Ser. 46, PAHs and the Universe: A Symposium to Celebrate the 25th Anniversary of the PAH Hypothesis (Les Ulis: EDP Sciences), 177
Cherchneff, I., Barker, J. R., & Tielens, A. G. G. M. 1992, ApJ, 401, 269
Clemett, S. J., Nakamura-Messenger, K., McKay, D. S., & Sandford, S. A. 2007, LPSC, 38, 2091
Cook, A. M., Ricca, A., Mattioda, A. L., et al. 2015, ApJ, 799, 14
Cruikshank, D. P., Wegryn, E., Dalle Ore, C., et al. 2008, Icar, 193, 334
Dartnell, L. R., Patel, M. R., Storrie-Lombardi, M. C., Ward, J. M., & Müller, J.-P. 2012, M&PS, 47, 806
Dixon, J. M., Taniguchi, M., & Lindsey, J. S. 2005, Photochem. Photobiol., 81, 212
Du, H., Fuh, R.-C. A., Li, J., Corkan, L. A., & Lindsey, J. S. 1998, Photochem. Photobiol., 68, 141
Ehrenfreund, P., D'hendecourt, L., Verstraete, L., et al. 1992, A&A, 259, 257
Ehrenfreund, P., Rasmussen, S., Cleaves, J., & Chen, L. 2006, AsBio, 6, 490
Eigenbrode, J. L., Summons, R. E., Steele, A., et al. 2018, Sci, 360, 1096
Faccinetto, A., Thomson, K., Ziskind, M., & Focsa, C. 2008, ApPhA, 92, 969
Föhn, M., Galli, A., Vorburger, A., et al. 2021, in 2021 IEEE Aerospace Conf. (50100) (Piscataway, NJ: IEEE), 1
Frenklach, M., & Feigelson, E. D. 1989, ApJ, 341, 372
Gavilan Marin, L., Bejaoui, S., Haggmark, M., et al. 2020, ApJ, 889, 101
Goesmann, F., Brinckerhoff, W. B., Raulin, F., et al. 2017, AsBio, 17, 655
Gredel, R., Carpentier, Y., Rouillé, G., et al. 2011, A&A, 530, A26
Groen, J., Deamer, D., Kros, A., & Ehrenfreund, P. 2012, OLEB, 42, 295
Grubisic, A., Trainer, M. G., Li, X., et al. 2021, IJMSp, 470, 116707
Gudipati, M. S., & Allamandola, L. J. 2004, ApJL, 615, L177
Hahn, J. H., Zenobi, R., & Zare, R. N. 1987, JAChS, 109, 2842
Halasinski, T. M., Salama, F., & Allamandola, L. J. 2005, ApJ, 628, 555
Hudgins, D. M., & Sandford, S. A. 1998, JPCA, 102, 344
Huisken, F., Rouillé, G., Steglich, M., et al. 2014, in Proc. IAU Symp. 297, The Diffuse Interstellar Bands, ed. J. Cami & N. Cox (Cambridge: Cambridge Univ. Press), 265
Joblin, C., Tielens, A. G. G. M., & Cherchneff, I. 2011, in EAS Publications Ser. 46, PAHs and the Universe: A Symposium to Celebrate the 25th Anniversary of the PAH Hypothesis (Les Ulis: EDP Sciences), 3
Kovalenko, L. J., Maechling, C. R., Clemett, S. J., et al. 1992, AnaCh, 64, 682
Leger, A., & Puget, J. L. 1984, A&A, 500, 279

Ligterink, N. F. W., Grimaudo, V., Moreno-García, P., et al. 2020, NatSR, 10, 9641
López-Puertas, M., Dinelli, B. M., Adriani, A., et al. 2013, ApJ, 770, 132
Maltseva, E., Mackie, C. J., Candian, A., et al. 2018, A&A, 610, A65
Managadze, G., Wurz, P., Sagdeev, R., et al. 2011, SoSyR, 44, 376
McCabe, M. N., Hemberger, P., Reusch, E., Bodi, A., & Bouwman, J. 2020, J. Phys. Chem. Lett., 11, 2859
McGuire, B. A. 2021, arXiv:2109.13848
McGuire, B. A., Loomis, R. A., Burkhardt, A. M., et al. 2021, Sci, 371, 1265
Meyer, S., Riedo, A., Neuland, M. B., Tulej, M., & Wurz, P. 2017, JMSp, 52, 580
Millan, M., Teinturier, S., Malespin, C., et al. 2022, NatAs, 6, 129
Öberg, K. 2016, Chem. Rev., 116, 9631
Oomens, J., Meijer, G., & von Helden, G. 2001, JPCA, 105, 8302
Plows, F. L., Elsila, J. E., Zare, R. N., & Buseck, P. R. 2003, GeCoA, 67, 1429
Riedo, A., Bieler, A., Neuland, M., Tulej, M., & Wurz, P. 2013, JMSp, 48, i
Riedo, A., Tulej, M., Rohner, U., & Wurz, P. 2017, RScI, 88, 045114
Rohner, U., Whitby, J. A., & Wurz, P. 2003, MeScT, 14, 2159
Ruiterkamp, R., Cox, N. L. J., Spaans, M., et al. 2005, A&A, 432, 515
Ruiterkamp, R., Halasinski, T., Salama, F., et al. 2002, A&A, 390, 1153
Sabbah, H., Bonnamy, A., Papanastasiou, D., et al. 2017, ApJ, 843, 34
Sabbah, H., Pomerantz, A. E., Wagner, M., Müllen, K., & Zare, R. N. 2012, Energy & Fuels, 26, 3521
Salama, F., & Allamandola, L. J. 1991, JChPh, 94, 6964
Salama, F., & Allamandola, L. J. 1992, Natur, 358, 42
Salama, F., & Ehrenfreund, P. 2013, in Proc. IAU Symp. 297 The Diffuse Interstellar Bands, ed. J. Cami & N. L. J Cox (Cambridge: Cambridge Univ. Press), 364
Salama, F., Galazutdinov, G. A., Krełowski, J., Allamandola, L. J., & Musaev, F. A. 1999, ApJ, 526, 265
Salama, F., Galazutdinov, G. A., Krełowski, J., et al. 2011, ApJ, 728, 154
Sephton, M. A., Waite, J. H., & Brockwell, T. G. 2018, AsBio, 18, 843
Spencer, M. K., Hammond, M. R., & Zare, R. N. 2008, PNAS, 105, 18096
Steglich, M., Bouwman, J., Huisken, F., & Henning, T. 2011, ApJ, 742, 2
Szczepanski, J., & Vala, M. 1993, Natur, 363, 699
Szopa, C., Freissinet, C., Glavin, D. P., et al. 2020, AsBio, 20, 292
Tielens, A. 2008, ARA&A, 46, 289
Tielens, A. G. G. M. 2013, RvMP, 85, 1021
Tulej, M., Riedo, A., Neuland, M. B., et al. 2014, Geostand. Geoanal. Res., 38, 441
Wurz, P., Lykke, K. R., Pellin, M. J., Gruen, D. M., & Parker, D. H. 1992, Vacuu, 43, 381
Yang, T., Kaiser, R. I., Troy, T. P., et al. 2017, AngCh, 56, 4515
Zolotov, M., & Shock, E. 1999, JGRE, 104, 14033